Ionics (2019) 25:5221–5228
https://doi.org/10.1007/s11581-019-03094-2

ORIGINAL PAPER

Mn-doped $FeF_3 \cdot 0.33H_2O$ with enhanced electrochemical performance as cathode materials for lithium-ion batteries

Yan Lu[1] · Si Huang[1] · Zhengyu Zhang[1] · Xinping Huang[1] · Lifang Lan[1] · Lu Lu[1] · Sheng Li[1] · Jun Li[1] · Chunyang Pan[1] · Fenghua Zhao[1]

Received: 29 April 2019 / Revised: 23 May 2019 / Accepted: 25 May 2019 / Published online: 5 June 2019

Abstract

Lithium-ion batteries with the $FeF_3 \cdot 0.33H_2O$ cathode material enable a high energy density and safety. However, a major challenge of $FeF_3 \cdot 0.33H_2O$ is its low conductivity. In this work, $Fe_{1-2x/3}Mn_xF_3 \cdot 0.33H_2O$ ($x = 0$, 0.01, 0.03, 0.05, and 0.07) are prepared via the solvent thermal method. Systematic investigations have studied the effect of Mn-doping on the physical and electrochemical properties. The results indicate that Mn-doping not only does not destroy the lattice structure of $FeF_3 \cdot 0.33H_2O$, but also reduces the resistance and improves the diffusion coefficient of lithium ion, which provide it with better electrochemical properties. $Fe_{0.98}Mn_{0.03}F_3 \cdot 0.33H_2O$ delivers much excellent cycling performance and rate capacity than other materials. It has a 284.2 mAh g^{-1} initial discharge capacity that remains at 258.9 mAh g^{-1} after 50 cycles at 0.1 C, giving the high capacity retention rate of 91.1%. Additionally, the initial discharge capacity of $Fe_{0.98}Mn_{0.03}F_3 \cdot 0.33H_2O$ is 245, 231, 217, and 203 mAh g^{-1} at 1, 2, 5, and 10 C in the voltage range of 1.5–4.5 V vs. $Li^{+/}Li$, respectively.

Keywords Cathode material · Lithium-ion batteries · Mn-doping · $FeF_3 \cdot 0.33H_2O$ · Electrochemical performance

Introduction

Lithium-ion batteries (LIBs) that can maintain a high energy density, high working voltage, and long lifespan are necessary for applications in portable electronics, electric vehicles, and large-scale energy storage [1–5]. However, the greatest challenge for battery technology is meeting the demand for high-capacity and safe batteries. Therefore, significant interest is directed toward developing high performance electrode materials, which is the key for maximizing the performance of lithium-ion batteries.

Considerable focus has been placed on investigating iron-based fluorides due to their high theoretical energy density (712 mAh g^{-1}, three electrons transfer), low costs, and safety, which provide it with great potential for use as cathode materials in high-capacity lithium-ion batteries [6, 7]. However, there are several issues for these materials such as strong ionic bonds, a wide band gap and poor conductivity, which result in a low material rate performance that limits practical applications [8, 9]. FeF_3 is a multiphase crystal that mainly includes the following: anhydrous FeF_3 [10], $FeF_3 \cdot 0.33H_2O$ [11], $FeF_3 \cdot 0.5H_2O$ [12], and $FeF_3 \cdot 3H_2O$ [13]. Meanwhile, researchers have found that $FeF_3 \cdot 0.33H_2O$ has the most stable crystal structure and the best electrochemical performance [14–16]. The structure of $FeF_3 \cdot 0.33H_2O$ belongs to the orthogonal crystal system, the hexagonal tungsten bronze phase, in which iron atoms and fluorine atoms form a hexagonal tunnel, and water molecules are in the middle of the hexagon tunnel. Furthermore, the pore channels are benefit to the entry and exit of lithium ions, while the water molecules in the middle are conducive to the stability of the structure and the improvement of the conductivity. Researchers believe that it is this unique structure that makes this material's electrochemical performance better than other iron fluoride-containing crystal water [17–21].

The methods, such as the ball mill method [22, 23], the liquid phase method [24, 25], the template method [26, 27], and the solvent thermal method [28, 29], can use to prepare the FeF_3 cathode material. The materials prepared by these different methods contain different crystal water. Moreover, the pure phase $FeF_3 \cdot 0.33H_2O$ can be directly synthesized by

✉ Jun Li
qhxylijun@gdut.edu.cn

[1] Faculty of Chemical Engineering and Light Industry, Guangdong University of Technology, Guangzhou 510006, China

the simple solvent thermal method. This method is more prone to industrial production due to the controllable preparation conditions and low production costs.

The materials prepared by the solvent thermal method exhibit their excellent morphology and crystal structure. Nevertheless, the pure phase has poor conductivity and the actual capacity is relatively low [30]. Solving the issues, the approaches are often applied to improve the electrochemical properties of the cathode material, primarily cationic doping [31] and surface coating [32]. However, surface coating has the defect of being uneven, which easily falls off with the collecting fluid in the process of circulation and reduces the circulation performance. Doping is an effective way to fabricate high-performance material. For example, $Fe_{1-x}Co_xF_3 \cdot 0.33H_2O$ nanomaterials using the liquid phase method are synthesized by Sun et al. [33]. The result explains that an excellent electrochemical performance could be achieved in cationic-doped $FeF_3 \cdot 0.33H_2O$ cathode material for lithium-ion batteries. Yang et al. [34] calculate that Ti-doping can expand the hexagonal cavity of $FeF_3 \cdot 0.33H_2O$ through the first-principles theory, thereby improving the electrical conductivity of $FeF_3 \cdot 0.33H_2O$. Therefore, one can expect that the performance of $FeF_3 \cdot 0.33H_2O$ can be improved by Mn-doping.

In this work, we report on a facile strategy for the synthesis of Mn-doped $FeF_3 \cdot 0.33H_2O$ to prepare $Fe_{1-2x/3}Mn_xF_3 \cdot 0.33H_2O$. The effects of different doping amounts on the physical and electrochemical properties are comprehensively investigated.

Experimental

Fabrication of $Fe_{1-2x/3}Mn_xF_3 \cdot 0.33H_2O$

$Fe_{1-2x/3}Mn_xF_3 \cdot 0.33H_2O$ ($x = 0$, 0.01, 0.03, 0.05, and 0.07) was prepared by the hydrothermal method. $Fe(NO_3)_3 \cdot 9H_2O$ and $(CH_3COO)_2Mn \cdot 4H_2O$ in a molar ratio of 1:0, 0.994:0.01, 0.98:0.03, 0.967:0.05, and 0.954:0.07 were dissolved in a polytetrafluoroethylene container containing ethanol, cetyl trimethyl ammonium bromide, and Tween 80. The mixture was continuously stirred until it was dissolved to obtain reddish brown solution, and 15 ml 40 wt.% HF solution was slowly added with stirring. After 30 min, the polytetrafluoroethylene container was placed in a hydrothermal reaction vessel and sealed and then heated at 120 °C for 6 h in a blast drying oven. After cooling to room temperature, the light pink precipitate was obtained. Next, the precipitate was washed 4 times with ethanol to remove the unreacted HF and water, and then dried at 120 °C for 3 h to obtain a dried powder. The dried and mixed reactant mixture was reground and then heated in a tube furnace at 230 °C for 3 h under high-purity Ar protection to obtain $Fe_{1-2x/3}Mn_xF_3 \cdot 0.33H_2O$.

Material characterizations

The X-ray diffusion (XRD) phase test of the synthesized samples was done with an XD-2 using a Cu K_α radiation source ($\lambda = 0.15405$ nm). All of the diffraction patterns were recorded at room temperature in the 2θ range from 10° to 80° with a scan rate of 4°/min and were operated at 36 KV and 20 mA. The morphological and crystalline structures of the samples were characterized by a scanning electron microscope (SEM, JSM-7001F, JEOL).

Electrochemical measurements

The electrochemical performance of the obtained particles was tested using a CR2032 coin-type cell. First, the active material $Fe_{1-2x/3}Mn_xF_3 \cdot 0.33H_2O$ (90 wt%), acetylene black (5 wt%), and polyvinylidene fluoride binder (5 wt%) were mixed and ground with N-methylpyrrolidone as a solvent to form a uniform slurry, which was coated on aluminum foil and dried under a vacuum at 120 °C for 24 h. Then, the foil was pressed and cut into disks, and a Celgard 2400 polypropylene microporous membrane were used as the separator and lithium foil were used as the negative electrode, respectively. The electrolyte consists of 1 M $LiPF_6$ in a mixture of ethylene carbonate (EC), dimethyl carbonate (DMC), and ethylene methyl carbonate (EMC) (volume ratio 1:1:1). The cells were assembled in an argon glove box.

The galvanostatic discharge-charge characteristics of the cells were performed over the potential range between 1.5 and 4.5 V (vs. Li/ Li^+) using a Blue battery tester system (CT2001A Wuhan, China) at different rates of 0.1–10 C at room temperature. The cyclic voltammetry (CV) tests were measured using a CHI600A electrochemical workstation under a scan rate of 0.5 mV s^{-1} between 1.5 and 4.5 V (vs. Li/ Li^+). Electrochemical impedance spectroscopy (EIS) tests were performed by using an electrochemical workstation in the frequency range of 100 to 10 mHz with the perturbation of 5 mV. All of the characterizations and electrochemical measurements were conducted at room temperature (25 °C).

Results and discussion

Figure 1 shows the XRD patterns of $Fe_{1-2x/3}Mn_xF_3 \cdot 0.33H_2O$ ($x = 0$, 0.01, 0.03, 0.05, and 0.07). Among all investigated samples, no obvious diffraction peaks for any impurities are detected, the major X-ray diffraction peaks at the 2θ angles of 13.8°, 23.6°, and 27.8°, matching the standard diffraction pattern of $FeF_3 \cdot 0.33H_2O$, are indexed as the (110), (002), and (220) crystal planes, respectively. The results indicate that Mn-doping still maintains the material's structure, which shows the orthorhombic structure of the Cmcm space group. Furthermore, with the increase of the Mn content, the

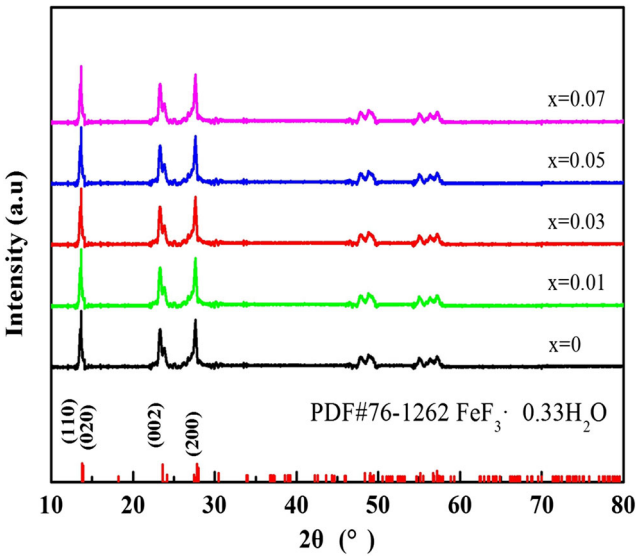

Fig. 1 XRD patterns of $Fe_{1-2x/3}Mn_xF_3{\cdot}0.33H_2O$ ($x = 0$, 0.01, 0.03, 0.05, and 0.07)

diffraction peaks have not only enhanced intensity but also sharp shape owing to a high crystallinity of the material. Additionally, no diffraction peaks of Mn are detected in the $Fe_{1-2x/3}Mn_xF_3{\cdot}0.33H_2O$ samples, indicating that Mn is effectively doped, but it does not change the lattice structure of the $FeF_3{\cdot}0.33H_2O$.

Figure 2 is SEM images of $Fe_{1-2x/3}Mn_xF_3{\cdot}0.33H_2O$ ($x = 0$, 0.01, 0.03, 0.05, and 0.07). The $FeF_3{\cdot}0.33H_2O$ exhibits a rod-like structure that is approximately 3–9-μm long and 0.5–2-μm wide and can be seen in Fig. 2a. The surfaces of the pure phase $FeF_3{\cdot}0.33H_2O$ particles are relatively smooth. By contrast, the surfaces of the Mn-doped sample particles are rough, and this can greatly increase the specific surface area of the particles, and could help promoting the penetration of the electrolyte, these factors result in enhancing the electrochemical performance [35, 36]. The comparison shows that the particle size of $Fe_{0.98}Mn_{0.03}F_3{\cdot}0.33H_2O$ is the smallest in $Fe_{1-2x/3}Mn_xF_3{\cdot}0.33H_2O$ ($x = 0$, 0.01, 0.03, 0.05 and 0.07). The electrode material with small particle size has larger specific surface area, and the electrolyte is more easily penetrated with the fastest ion diffusion rate. The SEM image reveals that it is effective to reduce the particle size and shorten the process of crystal growth via the Mn-doping. A smaller particle size can strongly reduce the resistance, possessing a superior electrochemical performance.

Figure 3 shows charge/discharge performance curves of $Fe_{1-2x/3}Mn_xF_3{\cdot}0.33H_2O$ ($x = 0$, 0.01, 0.03, 0.05, and 0.07) cathode material at 0.1 C. As shown in Fig. 3a, the pure phase $FeF_3{\cdot}0.33H_2O$ has a relatively low initial discharge specific capacity (234.8 mAh g^{-1}), which may be attributed to its poor conductivity. However, the doped samples have a high discharge specific capacity. The electrode can deliver the initial discharge capacities of 246.1, 284.2, 275.6, and 261.8 mAh g^{-1} when doping amounts are $x = 0.01$, 0.03, 0.05, and 0.07, respectively. Noticeably, the change of the discharge capacity is not linearly related to the increase of Mn content. The discharge capacity decreases when the doping amount reaches the maximum, which suggests that the Mn doping amount should not be too high. It is worth noting that the $Fe_{0.98}Mn_{0.03}F_3{\cdot}0.33H_2O$ cathode material possesses the highest discharge capacity. Figure 3b

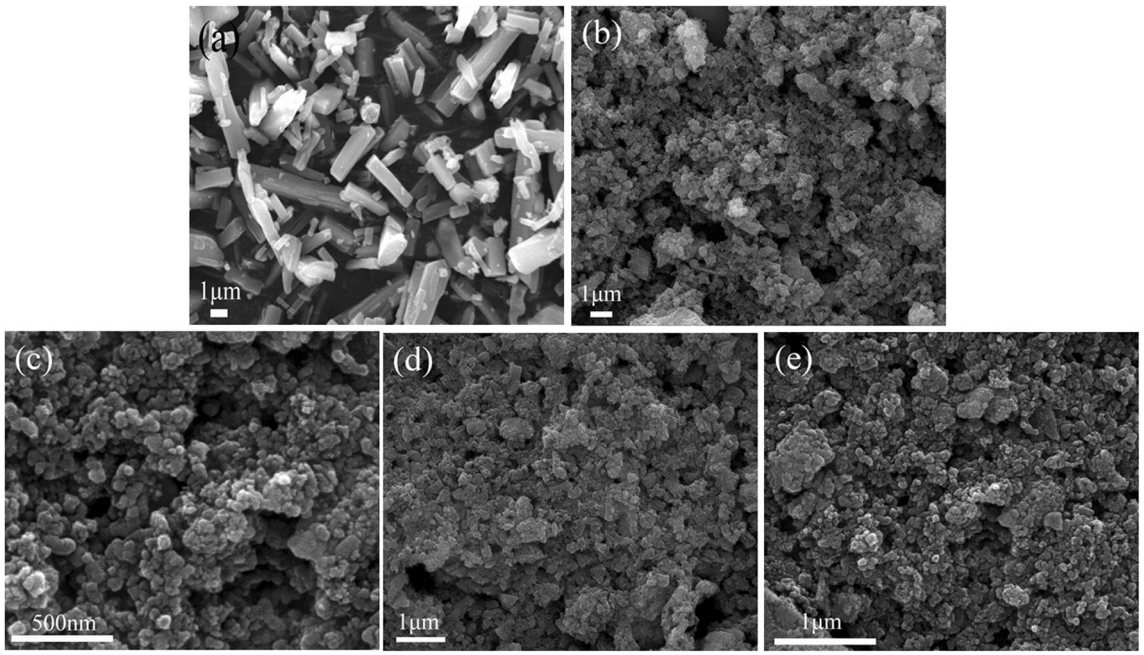

Fig. 2 SEM images of $Fe_{1-2x/3}Mn_xF_3{\cdot}0.33H_2O$: **a** $x = 0$, **b** $x = 0.01$, **c** $x = 0.03$, **d** $x = 0.05$, **e** $x = 0.07$

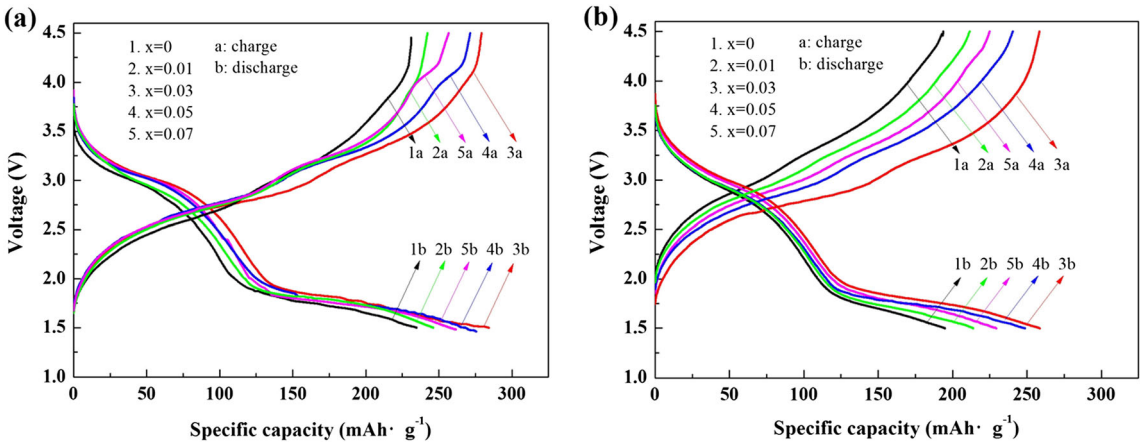

Fig. 3 Initial (**a**) and after 50 cycles (**b**) charge/discharge curves of $Fe_{1-2x/3}Mn_xF_3{\cdot}0.33H_2O$ ($x = 0$, 0.01, 0.03, 0.05, and 0.07) at 0.1 C

displays the discharge capacity of the pure phase $FeF_3{\cdot}0.33H_2O$ decreases to 194.9 mAh g^{-1}, retaining 83% of initial capacity after 50 cycles. The discharge capacities of $Fe_{1-2x/3}Mn_xF_3{\cdot}0.33H_2O$ ($x = 0.01$, 0.03, 0.05, and 0.07) remain at 216.8, 258.9, 246.9, and 232.7 mAh g^{-1}, and the capacity retention rates are 88.1%, 91.1%, 89.6%, and 88.9%, respectively. It shows a great cycling stability of Mn-doped material. The $Fe_{0.98}Mn_{0.03}F_3{\cdot}0.33H_2O$ cathode material exhibits an excellent cycling performance after 50 cycles. All these above features indicate that an improved electrochemical performance is achieved with moderate Mn-doping. On the one hand, Mn-doping can effectively reduce the size of $FeF_3{\cdot}0.33H_2O$ particles as well as the specific surface area so as to shorten the diffusion path length for Li^+ and electron transport. On the other hand, Mn^{2+} partially substituted Fe^{3+} reduces the band gap, which improves the conductivity of the material.

Rate performance of $Fe_{1-2x/3}Mn_xF_3{\cdot}0.33H_2O$ ($x = 0$, 0.01, 0.03, 0.05 and 0.07) from 0.1 to 10 C is presented in Fig. 4.

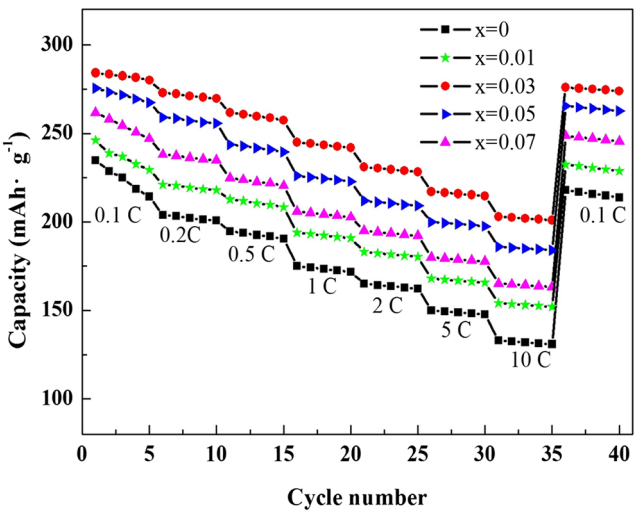

Fig. 4 Cyclic performances of $Fe_{1-2x/3}Mn_xF_3{\cdot}0.33H_2O$ ($x = 0$, 0.01, 0.03, 0.05, and 0.07) at different rates

The average discharge capacity at different rates is displayed in Fig. 5. Clearly, the higher discharge capacities of Mn-doped samples than that of $FeF_3{\cdot}0.33H_2O$ are achieved at different rates, suggesting good conductivity of Mn-doped samples. Besides, the lower discharge capacities of the five samples, can be obtained with the increasing of different rates (from 0.1 to 10 C), exhibiting different rate of reduction. Among them, $Fe_{0.98}Mn_{0.03}F_3{\cdot}0.33H_2O$, which shows the higher discharge capacity and the slowest rate of reduction, reaches the average discharge capacities of 282.3, 271.3, 259.6, 243.4, 229.6, 215.8, and 202.0 mAh g^{-1} at 0.1, 0.2, 0.5, 1, 2, 5, and 10 C rates, respectively. When the rate returned back to 0.1 C, the specific capacity of $Fe_{0.98}Mn_{0.03}F_3{\cdot}0.33H_2O$ can be quickly returned to 276.1 mAh g^{-1} with a capacity retention of 97.8%. At the first current density of 0.1 C, the discharge capacity of 5 discharge cycles deteriorates dramatically because the initial irreversible reaction results in irreversible capacity.

To evaluate the cycling performance of $FeF_3{\cdot}0.33H_2O$ and $Fe_{0.98}Mn_{0.03}F_3{\cdot}0.33H_2O$, the samples are cycled 50 times at

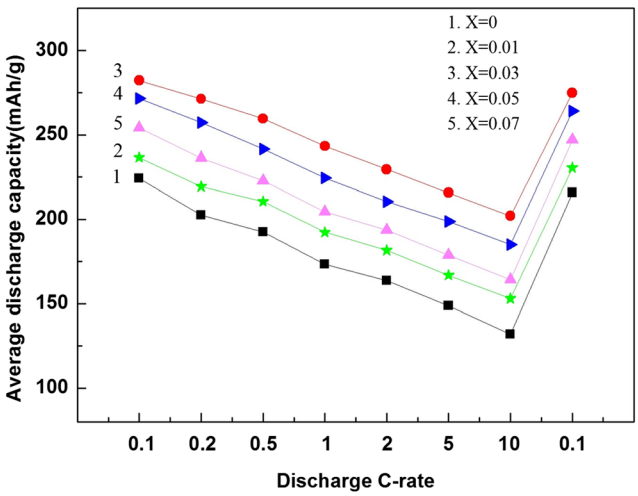

Fig. 5 The average values of discharge capacities at different C rates

1 C to obtain cycling performance curves, as shown in Fig. 6. The capacity loss in the first 10 times is obvious, which is caused by the occurrence of side reactions and the formation of the SEI film, leading to a partial irreversible capacity. The first discharge capacities of $Fe_{0.98}Mn_{0.03}F_3{\cdot}0.33H_2O$ and $FeF_3{\cdot}0.33H_2O$ are 245.2 and 175.3 mAh g^{-1}. After 50 cycles the samples maintain a capacity of 219.6 and 134.6 mAh g^{-1} with the capacity retention of 89.6% and 76.8%, respectively, and especially the coulombic efficiencies reach nearly 99%. The excellent cycling stability of $Fe_{0.98}Mn_{0.03}F_3{\cdot}0.33H_2O$ is attributed to the following: (i) Mn-doping effectively increases the unit cell volume by reducing the activation energy barrier required for Li^+ diffusion and increasing the Li^+ diffusion coefficient; and (ii) the size of $FeF_3{\cdot}0.33H_2O$ particles is reduced by Mn^{2+} partially substituted Fe^{3+} providing a transport channel for the insertion and conversion reaction of Li^+, which facilitates the migration of lithium ions and improves the conductivity of the material.

Figure 7 exhibits the CV curves of $Fe_{1-2x/3}Mn_xF_3{\cdot}0.33H_2O$ ($x = 0$, 0.01, 0.03, 0.05, and 0.07) obtained at the scanning voltage of 1.5 to 4.5 V and the scanning rate of 0.5 mV s^{-1}. In the CV curves, the peak in the positive direction of the ordinate axis is the oxidation peak, and that in the negative direction is the reduction peak. The potential difference between the two peaks reflects the polarization degree of the electrode. The electrode reaction process of FeF_3 in a lithium-ion battery is [37, 38].

$$FeF_3 + Li \rightarrow LiFeF_3 (4.5\text{–}1.7V) \quad (1)$$

$$LiFeF_3 + 2Li \rightarrow Fe + 3LiF (1.7\text{–}1.5V) \quad (2)$$

It can be seen from the figure that two pairs of redox peaks are observed, corresponding to the conversion between the Fe^{3+} and Fe^{2+} phases in the Li^+ insertion/extraction behaviors and the chemical transformation reaction between the Fe^{2+} and Fe^0 phases, which are consistent with Fig. 3. The potential interval of $Fe_{1-2x/3}Mn_xF_3{\cdot}0.33H_2O$ ($x = 0$, 0.01, 0.03, 0.05, and 0.07) are 1.07, 0.98, 0.61, 0.66, and 0.83 V, respectively, indicating that $Fe_{0.98}Mn_{0.03}F_3{\cdot}0.33H_2O$ ($\triangle E = 0.61$) has the smallest polarization.

Figure 8 shows the EIS curves of $Fe_{1-2x/3}Mn_xF_3{\cdot}0.33H_2O$ ($x = 0$, 0.01, 0.03, 0.05, and 0.07) cathode materials after 1 cycle, 20 cycles, and 50 cycles at 1 C. The EIS profiles exhibit a semicircle in the high frequency region and an oblique line in the low frequency region. The equivalent circuit model is shown in the figure, which shows that the fitted graph and the experimentally measured pattern match well. As showed in Table 1, the fitted values of the impedance spectra can be obtained by the relevant equivalent circuit model. In the equivalent circuit, R_s denotes the impedance of the electrode

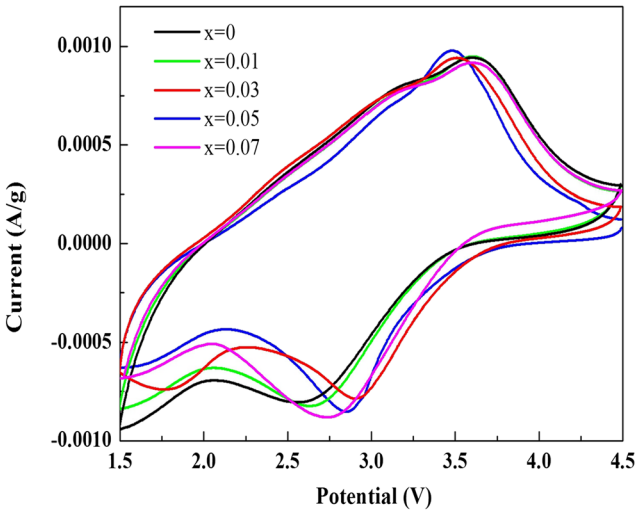

Fig. 7 CV curves of $Fe_{1-2x/3}Mn_xF_3{\cdot}0.33H_2O$ ($x = 0$, 0.01, 0.03, 0.05, and 0.07) at a scan rate of 0.5 mV s^{-1}

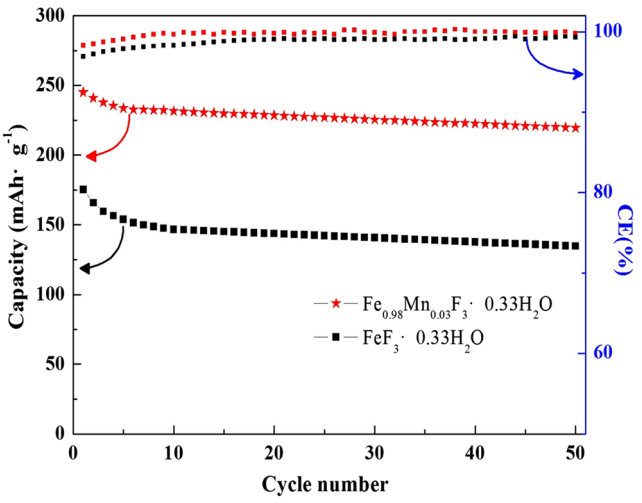

Fig. 6 Cyclic performances of $Fe_{0.98}Mn_{0.03}F_3{\cdot}0.33H_2O$ and $FeF_3{\cdot}0.33H_2O$ at 1 C and 1.5–4.5 V

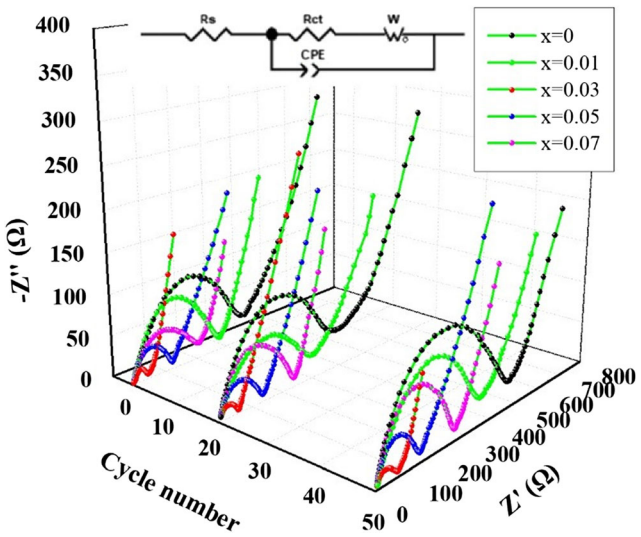

Fig. 8 EIS curves of $Fe_{1-2x/3}Mn_xF_3{\cdot}0.33H_2O$ ($x = 0$, 0.01, 0.03, 0.05, and 0.07) cathode materials after 1 cycle, 20 cycles, and 50 cycles at 1 C

Table 1 Simulated impedance parameters of $Fe_{1-2x/3}Mn_xF_3{\cdot}0.33H_2O$ ($x = 0$, 0.01, 0.03, 0.05, and 0.07)

Sample	R_s (Ω)			R_{ct} (Ω)		
	1st	20th	50th	1st	20th	50th
$x = 0$	7.298	7.865	8.256	367.52	399.10	468.95
$x = 0.01$	6.820	7.197	7.996	276.80	302.70	357.24
$x = 0.03$	3.405	5.083	6.895	46.964	59.093	70.142
$x = 0.05$	4.466	5.334	6.475	122.02	136.27	142.94
$x = 0.07$	5.901	6.108	6.294	209.09	238.32	265.84

system, R_{ct} represents the charge transfer impedance, CPE is used instead of the interface impedance, and W is the Warburg impedance of the solid phase diffusion, which is related to the diffusion dynamics of Li^+ in the solid lattice. It can be seen from the figure that there are no significant differences between the R_s values of the samples. Moreover, the R_s and R_{ct} values of the Mn-doped composites are lower than those of $FeF_3{\cdot}0.33H_2O$ with the increasing cycle number. Especially, the R_s and R_{ct} values of $Fe_{0.98}Mn_{0.03}F_3{\cdot}0.33H_2O$ show a minimal change. The R_{ct} values of $FeF_3{\cdot}0.33H_2O$ are 367.52, 399.10, and 468.95 Ω after 1 cycle, 20 cycles, and 50 cycles, respectively, while the R_{ct} values of $Fe_{0.98}Mn_{0.03}F_3{\cdot}0.33H_2O$ are 46.96, 59.09 and 70.14 Ω after 1 cycle, 20 cycles, and 50 cycles, respectively, much less than those of the $FeF_3{\cdot}0.33H_2O$. This phenomenon confirms that $Fe_{0.98}Mn_{0.03}F_3{\cdot}0.33H_2O$ presents minimum polarization when the electrode reaction occurs, which is consistent with the CV result. The smaller polarization is of benefit to the insertion and extraction of Li^+, effectively enhancing the stability of the positive electrode material. Therefore, benefiting from an appropriate amount of Mn-doping to reduce the charge transfer impedance, the electrochemical reversibility of the material can be improved.

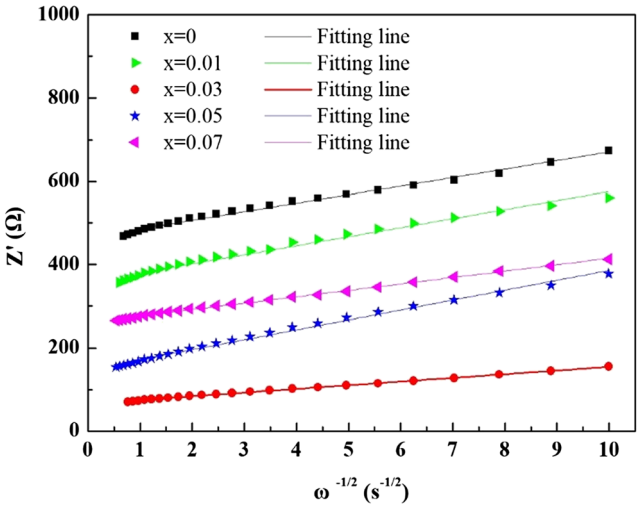

Fig. 9 Graph of Z_{re} plotted against $\omega^{-1/2}$ after 50 cycles for $Fe_{1-2x/3}Mn_xF_3{\cdot}0.33H_2O$ ($x = 0.01$, 0.03, 0.05, and 0.07) cathode material

Table 2 Electrochemical Kinetic Parameters of $Fe_{1-2x/3}Mn_xF_3{\cdot}0.33H_2O$ ($x = 0$, 0.01, 0.03, 0.05, and 0.07) after 50 cycles at 1 C

Samples	R_s (Ω)	R_{ct} (Ω)	D_{Li}^+ ($cm^2\ s^{-1}$)
$x = 0$	8.256	468.95	2.71×10^{-14}
$x = 0.01$	7.996	357.24	3.26×10^{-14}
$x = 0.03$	6.895	70.142	1.95×10^{-13}
$x = 0.05$	6.475	142.94	6.44×10^{-14}
$x = 0.07$	6.294	265.84	3.66×10^{-14}

Figure 9 illustrates the linear relationship between Z_{re} and the reciprocal square root of the lower angular frequencies $\omega^{-1/2}$. According to Eqs. 3 and 4 [39, 40], we can calculate the D_{Li}^+ of $Fe_{1-2x/3}Mn_xF_3{\cdot}0.33H_2O$ ($x = 0$, 0.01, 0.03, 0.05, and 0.07).

$$Z_{re} = R_S + R_{ct} + \sigma_w{\cdot}\omega^{-0.5} \tag{3}$$

$$D_{Li+} = \frac{R^2T^2}{2A^2n^4F^4C_{Li}^2\sigma_w{}^2} \tag{4}$$

Table 2 shows that the electrochemical kinetics parameters of $Fe_{1-2x/3}Mn_xF_3{\cdot}0.33H_2O$ ($x = 0$, 0.01, 0.03, 0.05, and 0.07) after 50 cycles at 1 C. The R_s values of $Fe_{1-2x/3}Mn_xF_3{\cdot}0.33H_2O$ ($x = 0.07$) is lower than those of the other materials, whereas it is clear that $Fe_{0.98}Mn_{0.03}F_3{\cdot}0.33H_2O$ shows the highest D_{Li+}, 1.95×10^{-13} $cm^2\ s^{-1}$, among all materials, which corresponds to its highest initial discharge specific capacity. This result indicates Mn-doping helps to improve the conductivity of the material and accelerate the charge transfer reaction at the electrode/electrolyte interface, possessing good multiplier performance. More importantly, the D_{Li+} increases from 10^{-14} $cm^2\ s^{-1}$ to 10^{-13} $cm^2\ s^{-1}$, suggesting that Mn-doping is beneficial to Li^+ stripping/embedding, which not only increases the conductivity of lithium ions, but also decreases the polarization, thus improving the reaction kinetics of the electrode.

Conclusion

In conclusion, the $Fe_{1-2x/3}Mn_xF_3{\cdot}0.33H_2O$ cathode material was successfully fabricated via the solvent thermal method. The capability and cycling stability of these doped materials have been improved. Notably, $Fe_{0.98}Mn_{0.03}F_3{\cdot}0.33H_2O$ exhibits a high capacity of 245.2 mAh g^{-1} and it still retains 219.6 mAh g^{-1} at 1 C even after 50 cycles, which are higher than those of $FeF_3{\cdot}0.33H_2O$, indicating that Mn-doping can improve the multiplier performance of $FeF_3{\cdot}0.33H_2O$. Meanwhile, the EIS results reveal the charge transfer resistance of $FeF_3{\cdot}0.33H_2O$ decreases greatly after Mn-doping. The $Fe_{0.98}Mn_{0.03}F_3{\cdot}0.33H_2O$ has highest Li^+ diffusion coefficient

(1.95×10^{-13} cm^2 s^{-1}). This outstanding battery performance of $Fe_{0.98}Mn_{0.03}F_3{\cdot}0.33H_2O$ can primarily be attributed to Mn-doping, which reduces the size of particles, thereby accelerating the diffusion rate and reducing the polarization of the electrochemical reaction. Therefore, $Fe_{0.98}Mn_{0.03}F_3{\cdot}0.33H_2O$ promises to be a cathode material for power lithium-ion batteries.

Funding information This work is supported by the Science and Technology Plan Foundation of Guangdong (201803030015), the Science and Technology Plan Foundation of Guangzhou (2017B010119002) and the Science and Technology Plan Foundation of Guangzhou (201704030031).

References

1. Xu K (2014) Electrolytes and interphases in Li-ion batteries and beyond. Chem Rev 114(23):11503–11618. https://doi.org/10.1021/cr500003w
2. Liu CF, Neale ZG, Cao GZ (2016) Understanding electrochemical potentials of cathode materials in rechargeable batteries. Mater Today 19(2):109–123. https://doi.org/10.1016/j.mattod.2015.10.009
3. Wu FX, Yushin G (2017) Conversion cathodes for rechargeable lithium and lithium-ion batteries. Energy Environ Sci 10(2):435–459. https://doi.org/10.1039/C6EE02326F
4. Goodenough JB, Park KS (2013) The Li-ion rechargeable battery, a perspective. J Am Chem Soc 135(4):1167–1176. https://doi.org/10.1021/ja3091438
5. Choi JW, Aurbach D (2016) Promise and reality of post-lithium-ion batteries with high energy densities. Nat Rev Mater 1(4):16013. https://doi.org/10.1038/natrevmats.2016.13
6. Badway F, Cosandey F, Pereira N, Amatucci GG (2003) Carbon metal fluoride nanocomposites, high-capacity reversible metal fluoride conversion materials as rechargeable positive electrodes for Li batteries. J Electrochem Soc 150(9):A1318–A1327. https://doi.org/10.1149/1.1602454
7. Hu JL, Zhang Y, Cao DP, Li CL (2016) Dehydrating bronze iron fluoride as a high capacity conversion cathode for lithium batteries. J Mater Chem A 4(41):16166–16174. https://doi.org/10.1039/C6TA05929E
8. Tan JL, Liu L, Hu H, Yang ZH, Guo HP, Wei QL, Yi X, Yan ZC, Zhou Q, Huang ZF, Shu HB, Yang XK, Wang XY (2014) Iron fluoride with excellent cycle performance synthesized by solvothermal method as cathodes for lithium ion batteries. J Power Sources 251:75–84. https://doi.org/10.1016/j.jpowsour.2013.11.004
9. Chu QX, Xing ZC, Tian JQ, Ren XB, Asiri AM, Alyoubi AO, Alamry KA, Sun XP (2013) Facile preparation of porous FeF_3 nanospheres as cathode materials for rechargeable lithium-ion batteries. J Power Sources 236:188–191. https://doi.org/10.1016/j.jpowsour.2013.02.026
10. Zhang LG, Ji SM, Yu LT, Xu XJ, Liu J (2017) Amorphous FeF_3/C nanocomposite cathode derived from metal–organic frameworks for sodium ion batteries. RSC Adv 7(39):24004–24010. https://doi.org/10.1039/C7RA03592F
11. Conte DE, Carlo LD, Sougrati MT, Fraisse B, Stievano L (2016) Operando Mössbauer spectroscopy investigation of the electrochemical reaction with Lithium in bronze-type $FeF_3{\cdot}0.33H_2O$. J Phys Chem C 120(42):23933–23943. https://doi.org/10.1021/acs.jpcc.6b06711
12. Ali G, Lee JH, Chang W, Cho BW, Jung HG, Nam KW, Chung KY (2017) Lithium intercalation mechanism into $FeF_3{\cdot}0.5H_2O$ as a highly stable composite cathode material. Sci Rep 7(42237). https://doi.org/10.1038/srep42237
13. Ma DL, Wang HG, Li Y, Xu D, Yuan S, Huang XL, Zhang XB, Zhang Y (2014) In situ generated FeF_3 in homogeneous iron matrix toward high-performance cathode material for sodium-ion batteries. Nano Energy 10:295–304. https://doi.org/10.1016/j.nanoen.2014.10.004
14. Jung H, Song H, Kim T, Lee JK, Kim J (2015) FeF_3 microspheres anchored on reduced graphene oxide as a high performance cathode material for lithium ion batteries. J Alloys Compd 647:750–755. https://doi.org/10.1016/j.jallcom.2015.06.191
15. Liu M, Wang XY, Zhang R, Liu L, Hu H, Wang Y, Wei SY (2018) Hollow porous $FeF_3{\cdot}0.33H_2O$ microspheres by $AlPO_4$ coating as a cathode material of Na-ion batteries. J Energy Storage 18:103–111. https://doi.org/10.1016/j.est.2018.04.026
16. Zhai JR, Lei ZY, Rooney D, Wang HG, Sun KN (2018) Self-templated fabrication of micro/nano structured iron fluoride for high-performance lithium-ion batteries. J Power Sources 396:371–378. https://doi.org/10.1016/j.jpowsour.2018.06.048
17. Wei SY, Wang XY, Liu M, Zhang R, Wang G, Hu H (2018) Spherical $FeF_3{\cdot}0.33H_2O$/MWCNTs nanocomposite with mesoporous structure as cathode material of sodium ion battery. J Energy Chem 27:573–581. https://doi.org/10.1016/j.jechem.2017.10.032
18. Li ZS, Wang BZ, Li CL, Liu JJ, Zhang WQ (2015) Hydrogen-bonding-mediated structural stability and electrochemical performance of iron fluoride cathode materials. J Mater Chem A 3:16222–16228. https://doi.org/10.1039/C5TA03327F
19. Rao RS, Pralong V, Varadaraju UV (2016) Facile synthesis and reversible lithium insertion studies on hydrated iron trifluoride $FeF_3{\cdot}0.33H_2O$. Solid State Sci 55:77–82. https://doi.org/10.1016/j.solidstatesciences.2016.02.008
20. Tang YW, An JL, Xing HX, Wang XY, Zhai B, Zhang F, Li GD (2018) Synthesis of iron-fluoride materials with controlled nanostructures and composition through a template-free solvothermal route for lithium ion batteries. New J Chem 42:9091–9097. https://doi.org/10.1039/C8NJ00932E
21. Li BJ, Cheng ZJ, Zhang NQ, Sun KN (2014) Self-supported, binder-free 3D hierarchical iron fluoride flower-like array as high power cathode material for lithium batteries. Nano Energy 4:7–13. https://doi.org/10.1016/j.nanoen.2013.12.003
22. Lee J, Kang B (2016) Novel and scalable solid-state synthesis of a nanocrystalline FeF_3/C composite and its excellent electrochemical performance. Chem Commun 52:9414–9417. https://doi.org/10.1039/C6CC03706B
23. Xu XP, Chen S, Shui M, Xu LX, Zheng WD, Shu J, Cheng LL, Feng L, Ren YL (2015) The differentiation of elementary polarizations of $FeF_3{\cdot}3H_2O$/C cathode material in LIB. Ionics 21(4):1003–1010. https://doi.org/10.1007/s11581-014-1244-7
24. Bai Y, Zhou XZ, Zhan C, Ma L, Yuan YF, Wu C, Chen MZ, Chen GH, Ni Q, Wu F, Shahbazian-Yassar R, Wu TP, Lu J, Amine K (2017) 3D hierarchical nano-flake/micro-flower iron fluoride with hydration water induced tunnels for secondary lithium battery cathodes. Nano Energy 32:10–18. https://doi.org/10.1016/j.nanoen.2016.12.017
25. Shen YQ, Wang XY, Hu H, Jiang ML, Wei SY, Bai YS (2016) A reversible conversion and intercalation reaction material for Li ion battery cathode. Mater Lett 180:260–263. https://doi.org/10.1016/j.matlet.2016.05.132
26. Ali G, Lee JH, Cho BW, Nam K, Ahn D, Chang W, Oh SH, Chung KY (2016) Probing the sodiation-desodiation reactions in nano-sized iron fluoride cathode. Electrochim Acta 191:307–316. https://doi.org/10.1016/j.electacta.2016.01.080
27. Li CL, Yin CL, Gu L, Dinnebier RE, Mu XK, Aken Peter A, Maier J (2014) An $FeF(3){\cdot}0.5H_2O$ polytype: a microporous framework

compound with intersecting tunnels for Li and Na batteries. J Am Chem Soc 44(46):11425–11428. https://doi.org/10.1016/j.electacta.2016.01.080

28. Sun HX, Zhou HC, Xu ZL, Ding J, Yang J, Zhou XY (2017) Preparation of anhydrous iron fluoride with porous fusiform structure and its application for Li-ion batteries. Microporous Mesoporous Mater 253:10–17. https://doi.org/10.1016/j.micromeso.2017.06.033
29. Li J, Fu LC, Xu ZW, Zhu JJ, Yang WL, Li DY, Zhou LP (2018) Electrochemical properties of carbon-wrapped FeF_3 nanocomposite as cathode material for lithium ion battery. Electrochim Acta 281:88–98. https://doi.org/10.1016/j.electacta.2018.05.158
30. Chen GH, Zhou XZ, Bai Y, Yuan YF, Li Y, Chen MZ, Ma L, Tan GQ, Hu JP, Wang ZH, Wu F, Wu C, Lu J (2019) Enhanced lithium storage capability of $FeF_3{\cdot}0.33H_2O$ single crystal with active insertion site exposed. Nano Energy 56:884–892. https://doi.org/10.1016/j.nanoen.2018.11.080
31. Liu M, Wang XY, Wei SY, Hu H, Zhang R, Liu L (2018) Cr-doped $Fe_2F_5{\cdot}H_2O$ with open framework structure as a high performance cathode material of sodium-ion batteries. Electrochim Acta 269:479–489. https://doi.org/10.1016/j.electacta.2018.02.159
32. Zhang Q, Sun C, Fan L, Zhang N, Sun K (2019) Iron fluoride vertical nanosheets array modified with graphene quantum dots as long-life cathode for lithium ion batteries. Chem Eng J 371:245–251. https://doi.org/10.1016/j.cej.2019.04.073
33. Sun B, Liu H, Munroe P, Ahn H, Wang GX (2012) Nanocomposites of CoO and a mesoporous carbon (CMK-3) as a high performance cathode catalyst for lithium-oxygen batteries. Nano Res 5(7):460–469. https://doi.org/10.1007/s12274-012-0231-4
34. Yang ZH, Zhang ZJ, Yuan YL, Huang XY, Chen XY, Wei SY (2016) First-principles study of Ti doping in $FeF_3{\cdot}0.33H_2O$. Curr Appl Phys 16(8):905–913. https://doi.org/10.1016/j.cap.2016.05.010
35. Wu F, Chen JZ, Li L, Zhao T, Chen RJ (2011) Improvement of rate and cycle performance by rapid polyaniline coating of a MWCNT/sulfur cathode. J Phys Chem C 115(49):24411–24417. https://doi.org/10.1021/jp207893d
36. Wang YG, Li HB, Xia YY (2006) Ordered whiskerlike polyaniline grown on the surface of mesoporous carbon and its electrochemical capacitance performance. Adv Mater 18(19):2619–2623. https://doi.org/10.1002/adma.200600445
37. Li C, Gu L, Tsukimoto S, Aken PA, Maier J (2010) Low-temperature ionic-liquid-based synthesis of nanostructured iron-based fluoride cathodes for lithium batteries. Adv Mater 22(33):3650–3654. https://doi.org/10.1002/adma.201000535
38. Li LP, Zhu JH, Xu MW, Jiang J, Li CM (2017) In situ engineering toward core regions: a smart way to make applicable FeF3@carbon nanoreactor cathodes for Li-ion batteries. ACS Appl Mater Interfaces 9(21):17992–18000. https://doi.org/10.1021/acsami.7b04256
39. Gao F, Tang ZY (2008) Kinetic behavior of $LiFePO_4$/C cathode material for lithium-ion batteries. Electrochim Acta 53:5071–5075. https://doi.org/10.1016/j.electacta.2007.10.069
40. Bai Y, Zhou XZ, Jia Z, Wu C, Yang LW, Chen MZ, Zhao H, Wu F, Liu G (2015) Understanding the combine effects of microcrystal growth and band gap reduction for $Fe_{(1-x)}Ti_xF_3$ nanocomposites as cathode materials for lithium-ion batteries. Nano Energy 17:140–151. https://doi.org/10.1016/j.nanoen.2015.08.006